



Preparation of g-C₃N₄ nanorod/InVO₄ hollow sphere composite with enhanced visible-light photocatalytic activities



Zengyu You^a, Yuxuan Su^a, Yang Yu^a, Hui Wang^a, Tian Qin^a, Fang Zhang^b, Qianhong Shen^{a,b,*}, Hui Yang^{a,b,*}

^a State Key Laboratory of Silicon Materials, School of Materials Science and Engineering, Zhejiang University, Hangzhou 310027, PR China

^b Zhejiang-California International NanoSystems Institute, Zhejiang University, Hangzhou 310058, PR China

ARTICLE INFO

Article history:

Received 3 February 2017

Received in revised form 22 April 2017

Accepted 3 May 2017

Available online 4 May 2017

Keywords:

g-C₃N₄

InVO₄

Nanorod

Hollow sphere

Photocatalysis

ABSTRACT

A novel g-C₃N₄ nanorod/InVO₄ hollow sphere composite was fabricated through a facile template-free method. The structure-property relationship was analyzed, and the formation mechanism of such structure and morphology was also proposed based on the observation from time-dependent morphology evolution. The results show that InVO₄ hollow spheres uniformly load on the surface of g-C₃N₄ nanorod and thus forming the heterojunction with an intimate interface. The bulk g-C₃N₄ experiences a possible peeling process to form the rod-like structure, during which the mass ratio of InVO₄ and ultraphonic process play a key role. Moreover, bubble-template is believed to determine the formation of InVO₄ hollow sphere. Owing to this unique structure and morphology, the enhanced visible-light photocatalytic activities are achieved because of the synergistic effect of light harvesting, high transfer efficiency and enhanced separation efficiency of photo-generated carriers. And more importantly, this fabrication method combines heterojunction constructing with morphology controlling of g-C₃N₄ in one step, and thus may supply a new idea for the preparation of other g-C₃N₄ based composites.

© 2017 Elsevier B.V. All rights reserved.

1. Introduction

Semiconductor photocatalysis technology which utilize solar energy as a driving force has been emerging to be a promising way to solve the energy and environment problems because of its advantages of renewability, cleanness and safety [1,2]. In the past few decades, TiO₂ as a main photocatalyst has been widely studied and successfully implemented commercial applications. However, only the UV light with a wavelength less than about 388 nm, which is only a small part (3–5%) of solar spectrum, can excite electrons in the valence band of TiO₂. Therefore, many new photocatalysts with visible-light driven photocatalytic activities have been developed and become a very hot research topic in photocatalysis field.

In recent years, graphitic carbon nitride (g-C₃N₄) has stimulated intensive interest in the field of photocatalysis because of its 2D structure, extraordinary stability, visible-light response (with a bandgap of 2.7 eV) and tunable electronic structure [3–7]. As a

metal-free photocatalyst, g-C₃N₄ is composed of C and N which are two of the most abundant elements on this planet. Besides, g-C₃N₄ can be simply prepared by the thermal condensation of several low-cost nitrogen-rich precursors such as cyanamide [7], dicyandiamide [8,9], melamine [10,11], urea [12] and mixtures thereof [13], which make it a more accessible and promising photocatalyst. However, the bulk g-C₃N₄ still suffered from a few drawbacks such as relative low visible light harvesting, small specific surface area, rapid recombination of photo-generated charge carriers and low migration efficiency, therefore restricting its further utilization [14–16]. Much work has been performed, such as element doping [17,18], introducing vacancy [19] and constructing heterojunction between g-C₃N₄ and other semiconductors or noble metals, to solve the above problems [20–25]. Besides, nanostructures of g-C₃N₄ with high specific surface area such as quantum dots [26], nanorods [27,28] and nanosheets [29] have been developed in recent years. For instance, Sun et al. [30] prepared uniform g-C₃N₄ hollow sphere with a thickness ranging from 56 nm to 85 nm and Li et al. [31] fabricated g-C₃N₄ nanorod with an average diameter of 260 nm. These special nanostructures resulted in high specific surface area, enhanced light harvesting and low recombination efficiency of photo-generated electron-hole pairs, therefore increasing photocatalytic activities of g-C₃N₄.

* Corresponding authors at: State Key Laboratory of Silicon Materials, School of Materials Science and Engineering, Zhejiang University, Hangzhou 310027, PR China.

E-mail addresses: s.qianhong@163.com (Q. Shen), [\(H. Yang\).](mailto:yanghui@zju.edu.cn)

Besides of g-C₃N₄, InVO₄ was also proved to be another promising visible light responding photocatalyst [32,33]. Much work has been performed on the morphology of InVO₄ nanocrystals. Chen et al. [34] successfully synthesized various InVO₄ powders in the shape of rod-like, cubic-like, brick-like and irregular particle through a hydrothermal method. Zhang et al. [35] have confirmed that the crystallinity, particle size, morphology of the InVO₄ nanoparticles can be controllable regulated to achieve high photocatalytic activity. Especially, the control of morphology and size of photocatalysts can regulate the position of energy band to obtain higher redox ability [36,37]. Recently, nano InVO₄ was adopted to combine with g-C₃N₄ to form heterojunctions because of their well-matched energy band structure, leading to the enhancement of photocatalytic activity for air purification or hydrogen production under visible light irradiation [38].

Herein, a novel g-C₃N₄/InVO₄ composite containing g-C₃N₄ nanorod and InVO₄ hollow nano-sphere was fabricated through a facile template-free hydrothermal process. The InVO₄ hollow nanospheres are dispersed on the surface of g-C₃N₄ nanorod with an intimate interface after an annealing process. With such a unique structure, the as-prepared samples exhibits significantly improved performance compared with g-C₃N₄, InVO₄ and bulk g-C₃N₄/InVO₄ composite. The synergistic effect of light harvesting, high transfer efficiency and enhanced separation efficiency of photo-generated carriers is believed to be the reason for the enhancement of photocatalytic activity. The formation mechanism was proposed based on observation from time-dependent morphology evolvement.

2. Experimental

2.1. Materials

All the chemicals (AR grade) in this work, including cyanamide, sodium metavanadate (NaVO₃·2H₂O), Indium nitrate (In(NO₃)₃·4.5H₂O), methylene blue (MB) and tetracycline (TC) were purchased from Aladdin Reagent Co. Ltd. and used without any further purification. 5, 5-dimethyl-1-pyrroline-N-oxide (DMPO) was obtained commercially from Sigma-Aldrich (for ESR-spectroscopy).

2.2. Synthesis of photocatalysts

2.2.1. Synthesis of g-C₃N₄

Graphitic carbon nitride (g-C₃N₄) was synthesized through a thermal condensed process [7]. Firstly, a certain amount of cyanamide was placed in a semi-covered alumina crucible followed by being put into a tube furnace. Then the cyanamide was heated to 550 °C in air with a heating rate of 2.2 °C/min. After roasting at 550 °C for 4 h, the g-C₃N₄ was obtained.

2.2.2. Synthesis of g-C₃N₄/InVO₄ composites

The g-C₃N₄/InVO₄ composite was synthesized via a hydrothermal procedure followed by an annealing process. A measured amount of as-prepared bulk g-C₃N₄ and NaVO₃·2H₂O were put into a 100 ml glass beaker with 50 ml deionized water. After being drastic stirred for 10 min, the mixture was ultrasonicated for 20 min. Followed by another 10 min drastic stirring, In(NO₃)₃·4.5H₂O was put into the system drop by drop to a molar ratio of V³⁺:In⁵⁺ = 1:1, and then the mixture was stirred for another 30 min. The resultant was transferred to a 100 ml Teflon-lined steel autoclave, which was heated in an oven at 140 °C for 12 h. Subsequently, the precipitate was collected and washed by centrifugation with deionized water and ethyl alcohol two times respectively, and then dried at 60 °C for 6 h. Finally, after annealing at 500 °C for 1 h, g-C₃N₄/InVO₄ composite (denoted as RCN/SI) was obtained and then grounded for further use. As-prepared composites with expected InVO₄ mass fraction

of 20%, 40%, 50% and 60% were denoted as RCN/SI-20, RCN/SI-40, RCN/SI-50 and RCN/SI-60, respectively. For comparison, bulk g-C₃N₄/InVO₄ composite (denoted as BCN/NI) was fabricated through the similar method without the ultrasound process, and the pure InVO₄ was also synthesized by the similar procedure in the absence of g-C₃N₄. The pristine g-C₃N₄ experienced the same procedure without adding NaVO₃·2H₂O and In(NO₃)₃·4.5H₂O (denoted as CN).

2.3. Characterization

X-ray powder diffractometer (XRD, APEXII, Bruker, Germany) was used to identify the crystal structure of the obtained powders using Ni-filtered Cu Ka radiation ($\lambda = 0.1542$ nm). The 2 theta ranges from 10° to 80° in steps of 0.02°. Field emission scanning electron microscopy (SEM, SU-70, Hitachi, Japan) was used to investigate the morphology of samples. Further morphological and structural characterizations were based on field emission transmission electron microscopy and high-resolution transmission microscopy (TEM and HRTEM, Tecnai G2 F20 S-TWIN, FEI, USA) observation. UV-vis diffuse reflectance spectra (DRS) were obtained on a UV-vis spectrophotometer (DRS, Cary 5000, Agilent, USA) equipped with an integrating sphere. BaSO₄ acted as a reference and the absorption spectra were further calculated using the Kubelka-Munk function. The photoluminescence emission spectra and time-resolved fluorescence decay spectra of as-prepared samples were detected on a fluorescence lifetime and steady-state spectrometer (FLS920, Edinburgh, UK). In detail, the PL emission spectra were obtained at an excitation wavelength of 325 nm with a Xe lamp, and the PL decay spectra were recorded at an excitation wavelength of 405 nm with a nanosecond pulse laser.

2.4. Evaluation of photocatalytic activity

The photocatalytic activities of as-prepared samples were evaluated by the degradation of methylene blue (MB) [39] and tetracycline (TC) [40] in aqueous solution under visible light irradiation. For MB degradation, the light source is a 35 W metal-halide lamp (Philips) with a 420 nm UV-cutoff filter. The lamps were located 12 cm away from the surface of reaction solution (about 5 mW cm⁻²). In each experiment, 50 mg of a photocatalyst was dispersed in MB (100 ml, 10 mg L⁻¹) aqueous solution. Prior to irradiation, the solution was continuously stirred in the dark for 2 h to reach adsorption-desorption equilibrium between the MB and the photocatalyst. During the photocatalytic reaction, the solution were kept magnetically stirring, and 4 ml of the mixture was collected at 30 min intervals followed by centrifugation (10,000 rpm, 5 min) to remove the photocatalyst. The process of TC degradation was similar to that of MB. The light source was offered by a 300 W Xe lamp (Perfect Light Co. Ltd.). In each experiment, 30 mg of a photocatalyst was dispersed in TC (100 ml, 15 mg L⁻¹) aqueous solution. The concentration of MB and TC was determined by monitoring the change of absorbance at 663 nm and 356 nm respectively using a UV-vis spectrophotometer (UV-vis Abs, UV-4100, Hitachi, Japan).

2.5. Photoelectrochemical measurements

Electrochemical impedance spectroscopy (EIS) was performed on an electrochemical station (CHI 660E, Chenhua, China) in a conventional three electrode configuration with a Pt foil as the counter electrode and an Ag/AgCl electrode as the reference electrode. The as-prepared samples were deposited on fluorinated-tin-oxide (FTO) conducting glasses (1.5 cm × 0.75 cm) as the working electrode. A 300 W Xe arc lamp through a 420 nm UV-cutoff filter served as a light source and 0.5 M Na₂SO₄ aqueous solution served as electrolyte. The frequency ranged from 5×10^{-2} to 10^5 and the initial potential was 0 V. The photoelectric current (PC) response was

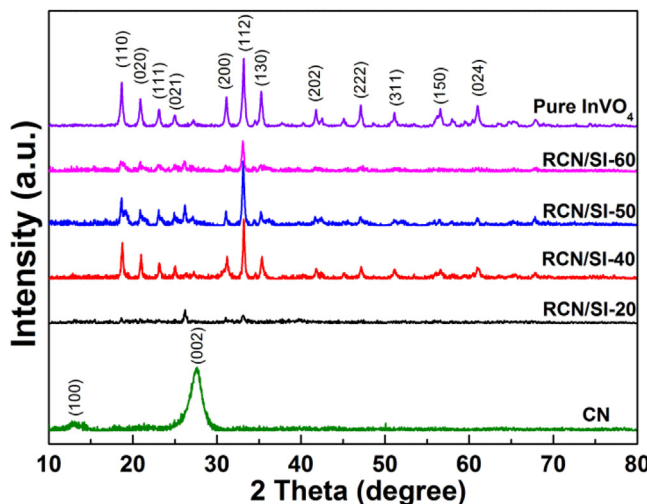


Fig. 1. XRD patterns of CN, pure InVO₄ and g-C₃N₄/InVO₄ composites.

obtained with the same electrochemical station (light on/off cycles: 40 s).

2.6. Active species trapping experiments

Isopropanol (IPA) and benzoquinone (BQ) were involved in MB photocatalytic degradation reaction system as the scavengers of hydroxyl radical ($\cdot\text{OH}$) and superoxide radical ($\cdot\text{O}_2^-$) respectively to elucidate the photocatalysis mechanism. The concentration of IPA and BQ were 2.0 mmol L⁻¹ and 0.1 mmol L⁻¹ respectively. The measurement was similar to the former photocatalytic activity experiment except that scavengers were added before visible-light irradiation. Additionally, electron spin resonance (ESR, ESRA-300, Bruker, Germany) signals were recorded by the probe molecular 5, 5-dimethyl-1-pyrroline-N-oxide (DMPO) under visible-light irradiation ($\lambda > 420$ nm). Samples for ESR measurement were prepared by mixing the as-prepared samples in 80 mM DMPO solution. Aqueous dispersion was used for DMPO- $\cdot\text{OH}$ and methanol dispersion was used for DMPO- $\cdot\text{O}_2^-$.

3. Results and discussion

3.1. Structure and morphology

The crystal structure of CN, pure InVO₄ and g-C₃N₄/InVO₄ composites were characterized by XRD. As shown in Fig. 1, two pronounced diffraction peaks are observed at 13.2° and 27.6° respectively. The former peak is indexed as the (110) plane corresponding to in-plane structural packing motif of tri-s-triazine units, and the diffraction peak at 27.6° is corresponded to interlayer stacking of the conjugated aromatic systems [7]. While for pure InVO₄, the characteristic peaks match well with standard card (JCPDS 71-1689). The main diffraction peaks of g-C₃N₄/InVO₄ composites did not change obviously, indicating that the fabrication process did not destroy the main structure of both of the counterpart.

The morphology and structure were directly observed by SEM and TEM. As shown in Fig. 2a, CN has bulk morphology. With mass ratio of InVO₄ reaches to 20% and 40%, it can be observed that InVO₄ nanoparticles are deposited on the surface of bulk-like g-C₃N₄ (Fig. 2b and c). Meanwhile, a small amount of rod-like g-C₃N₄ is found in Fig. 2c. With the mass ratio of InVO₄ rises to 50% and 60% (Fig. 2d and e), g-C₃N₄ exhibits a rod-like morphology with a diameter of about 100 nm. While the InVO₄ have a spherical morphology with a diameter of 30–50 nm and are deposited on the surface of g-C₃N₄ nanorod with intimate junction structure. How-

ever, for the g-C₃N₄/InVO₄ composite containing 50% InVO₄, which was fabricated without ultrasonication process (Fig. 2f), g-C₃N₄ appears porous monolithic structure with InVO₄ nanoparticles dispersed on it. Hence, the formation of g-C₃N₄ nanorod/InVO₄ sphere composite is believed to be related to both InVO₄ content and ultrasonication process. Besides, the pure InVO₄ is aggregation of nanoparticles with microsphere morphology, as shown in Fig. S1.

The morphology and structural details of g-C₃N₄ nanorod/InVO₄ sphere composites were investigated by TEM and HRTEM observation. Fig. 3a shows the overview of RCN/SI-50, from which nanorod-like g-C₃N₄ and InVO₄ hollow spheres can clearly be observed. InVO₄ hollow spheres with a diameter of about 50 nm are dispersed on g-C₃N₄ nanorod, coinciding with the results from SEM images. Furthermore, the composite was investigated by HRTEM images as shown in Fig. 3b. It can be seen that the shell of InVO₄ hollow spheres has a thickness of about 10 nm and exhibits the (110) facet with a spacing of 0.472 nm. Moreover, the calculated d value of 0.327 nm corresponds to the (002) crystallographic plane of g-C₃N₄ [41]. There is an obvious interface formed between g-C₃N₄ and InVO₄. Besides the nanorod/hollow sphere structure, the perfect crystalline quality and the clear interface between g-C₃N₄ and InVO₄ would facilitate the separation of the photo-generated charge carriers.

3.2. Formation mechanism of g-C₃N₄ nanorod/InVO₄ hollow sphere composite

To investigate the formation mechanism of g-C₃N₄ nanorod/InVO₄ hollow sphere composite, the time-dependent morphologies of the composite with InVO₄ mass ratio of 50% were investigated. As shown in Fig. 4a, at the beginning of the hydrothermal reaction, g-C₃N₄ appears to be a bulk-like morphology with lamellar and porous structure. After hydrothermal treatment for 2 h, as shown in Fig. 4b, most of the g-C₃N₄ still keep the lamellar and porous structure, while some sticking nanorod-like structure can also be found, indicating that bulk-like g-C₃N₄ begins to change to time of 2 h proving the tendency of formation of g-C₃N₄ single-nanorod. After a further prolonged reaction time to 8 h (Fig. 4d), g-C₃N₄ single-nanorod with a diameter of about 100 nm are obtained.

It has been illustrated that ultrasonication process plays a key role in the formation of g-C₃N₄ nanorods. As shown in Fig. 2, g-C₃N₄ prefers to grow to bulk-like morphology during hydrothermal if there is no ultrasonication process. In addition, when the content of InVO₄ are 20% and 40%, there are barely no rod-like g-C₃N₄ appear even treated through a ultrasonication process, revealing that the content of InVO₄ is also crucial to the formation of g-C₃N₄ nanorods. VO₃⁻ ions may insert into the layered g-C₃N₄ framework with assistance of ultrasonication process, and then go on combining with In³⁺ ions. In contrast, VO₃⁻ ions will tend to stay outside, as shown in Scheme 1. A similar phenomenon have been reported in Ni(OH)₂/g-C₃N₄ nanohybrids [42]. Furthermore, g-C₃N₄ nanorods can be formed through a “peeling” process with the assistance of nucleation and growth of InVO₄ when the mass ratio of InVO₄ reaches a certain mount.

The formation mechanism of InVO₄ hollow spheres is investigated by TEM analysis. It can be seen from Fig. 5a that the InVO₄ hollow spheres cannot be observed at the beginning of the hydrothermal reaction. However, when the reaction time prolonged to 2 h, regular amorphous InVO₄ hollow spheres appear (Fig. 5b). In the previous work, it has been confirmed that g-C₃N₄ can release NH₃ due to its thermal decomposition during the hydrothermal process [38]. Therefore, the most possible reason for the formation of InVO₄ hollow spheres is considered that NH₃ produced from g-C₃N₄ under hydrothermal conditions is served as a template for the growth of InVO₄.

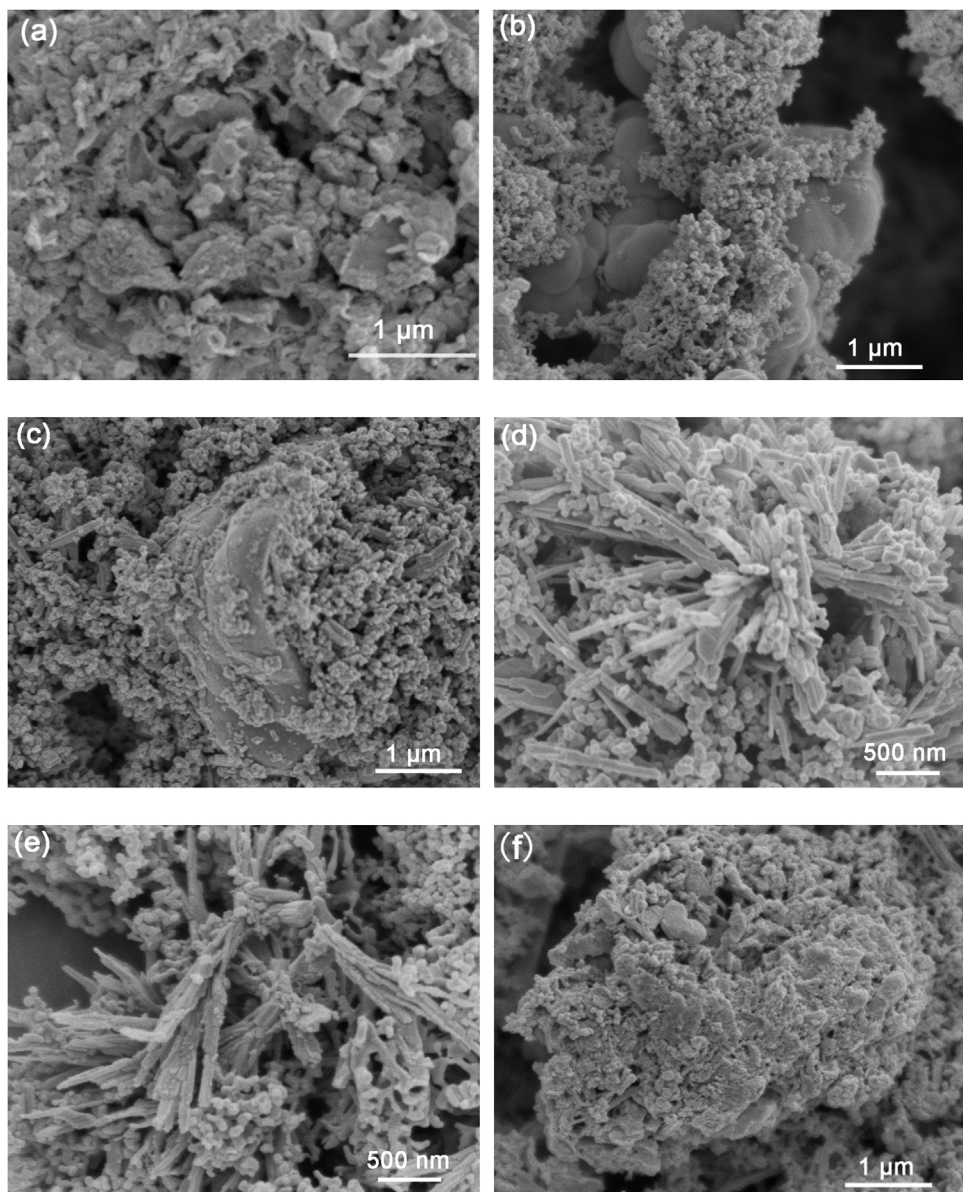


Fig. 2. SEM images of (a) CN, (b) RCN/SI-20, (c) RCN/SI-40, (d) RCN/SI-50 (e) RCN/SI-60 and (f) BCN/NI-50.

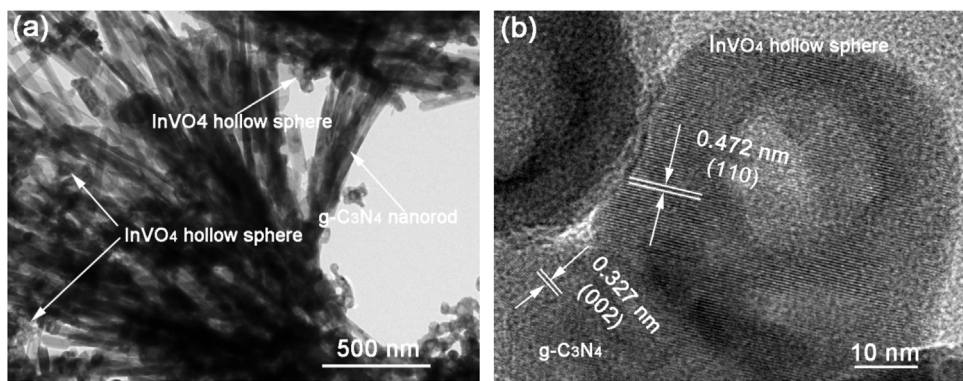


Fig. 3. (a) TEM and (b) HRTEM images of RCN/SI-50.

Based on the above analysis, the formation mechanism of g-C₃N₄ nanorod/InVO₄ hollow sphere structures is believed to involve the following processes (**Scheme 1**): a) At the first step

before hydrothermal reaction, VO₃⁻ ions insert into the layered g-C₃N₄ framework through stirring and ultrasonication conditions. The content of VO₃⁻ ions and ultrasonication process are two cru-

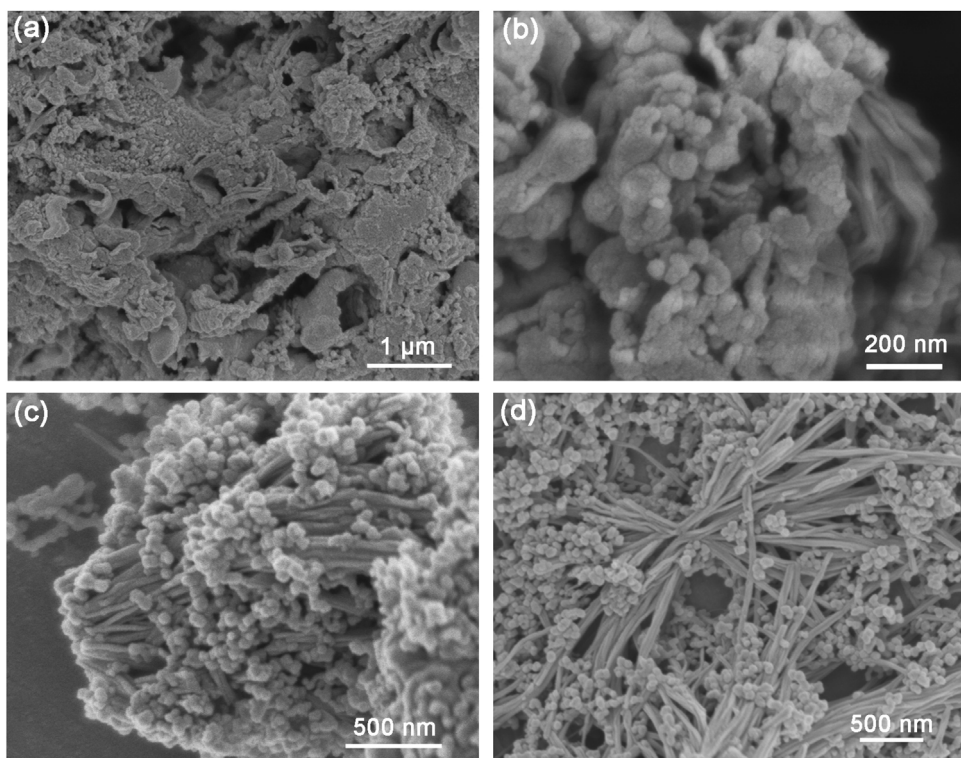
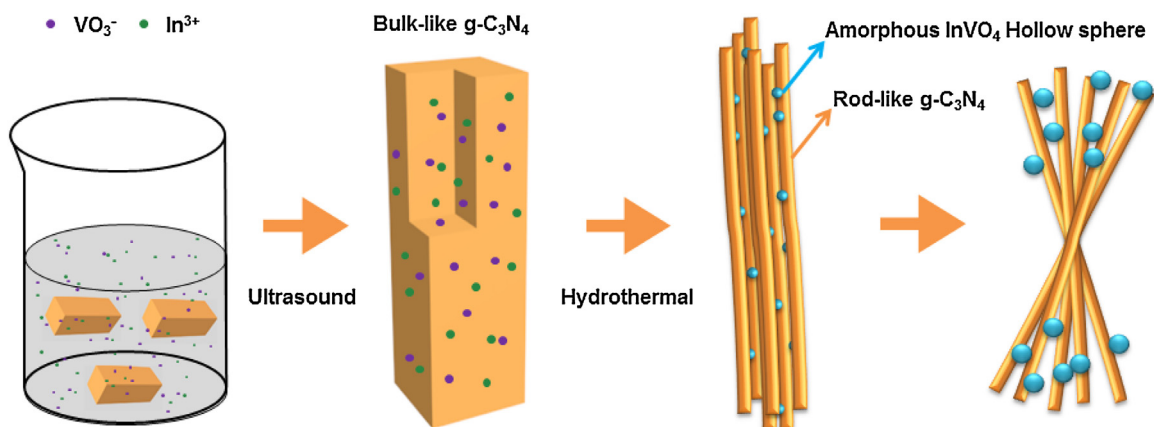


Fig. 4. SEM images for different hydrothermal reaction time: (a) 0 h, (b) 2 h, (c) 4 h and (d) 8 h.



Scheme 1. The schematic illustration of the formation of $\text{g-C}_3\text{N}_4$ nanorod/ InVO_4 hollow sphere composites.

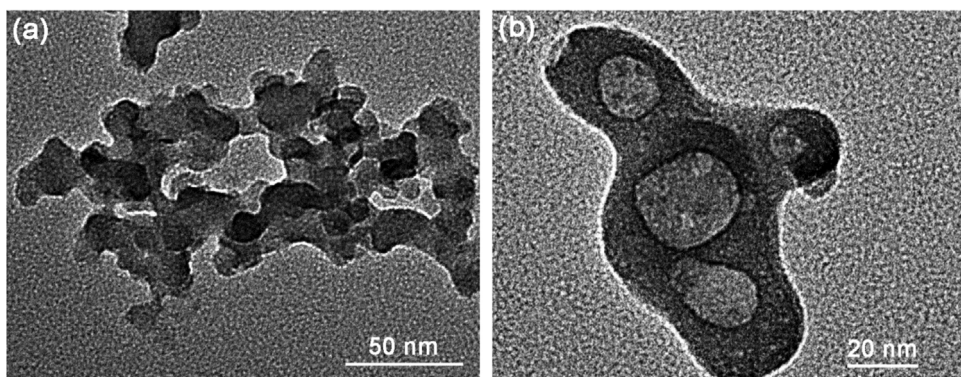


Fig. 5. TEM images for different hydrothermal reaction time: (a) 0 h and (b) 2 h.

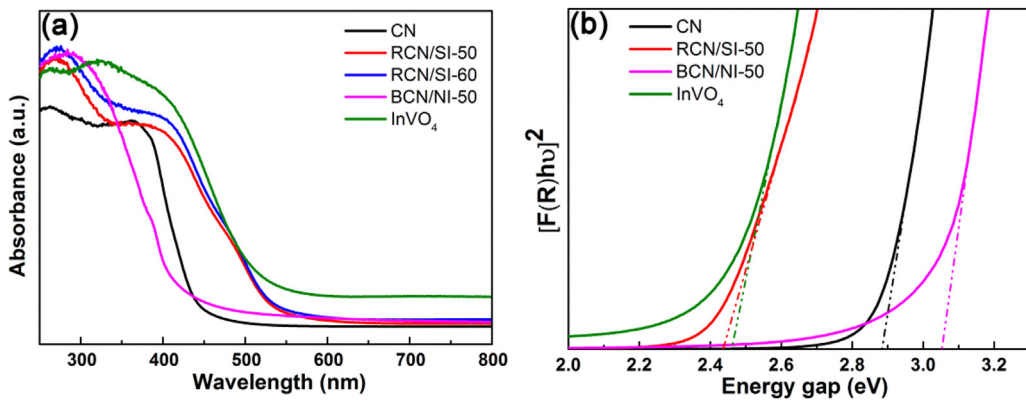


Fig. 6. (a) UV-vis DRS spectra of CN, RCN/SI-50, RCN/SI-60, BCN/NI-50 and pure InVO₄; (b) Band gap of CN, RCN/SI-50, BCN/NI-50 and InVO₄.

cial factors in this step, which is decisive for the formation of g-C₃N₄ nanorods. b) During the hydrothermal reaction, VO₃⁻ ions are combined with In³⁺ ions between the g-C₃N₄ layers to form initial amorphous InVO₄ nanoparticles. Meanwhile, NH₃ will be released as a result of thermal decomposition of g-C₃N₄. With the assistance of this NH₃ template, amorphous InVO₄ nanoparticles grow to hollow spherical nanostructure. Furthermore, g-C₃N₄ could change from bulk-like morphology to rod-like morphology through a peeling process caused by the growth of InVO₄. c) During the following annealing process, amorphous InVO₄ turns into orthorhombic phase. Therefore, the joint action of peeling effect and NH₃ template assistance is believed to be a formation mechanism for g-C₃N₄ nanorod/InVO₄ hollow sphere heterojunctions.

3.3. Optical properties

The g-C₃N₄/InVO₄ composites, pure g-C₃N₄ and pure InVO₄ were analyzed by UV-vis diffuse reflectance spectra. Fig. 6a illustrates that g-C₃N₄ holds an absorption edge of around 430 nm. BCN/NI-50 samples possess blue-shifted absorption edge compared with CN, which indicated that the band gap of photocatalysts enlarged owing to the size change of loaded InVO₄. InVO₄ nanoparticles have a larger band gap than that of InVO₄ microspheres [43]. However, g-C₃N₄ nanorod/InVO₄ hollow spheres (RCN/SI-50 and RCN/SI-60) show a distinct red-shift compared with CN. In addition, by extrapolating the linear portion of [F(R)hv]² versus (hv) curves (Fig. 6b), the Eg's of CN, RCN/SI-50, BCN/NI-50 and InVO₄ are estimated to be about 2.88 eV, 2.43 eV, 3.05 eV, and 2.45 eV respectively, indicating that g-C₃N₄ nanorod/InVO₄ hollow spheres nanostructure is more light harvesting in visible light region than CN and bulk g-C₃N₄/InVO₄ composite.

The observed PL emission peak is attributed to the radiative recombination process of either self-trapped excitons, so a lower PL intensity indicates a better charge separation of photo-generated electron-hole carriers [44]. As shown in Fig. 7a, CN has a strong emission peak at around 460 nm with much more higher intensity than that of other samples, indicating that photo-generated electron-hole pairs of CN recombine rapidly. While pure InVO₄ has an emission peak between 520 and 530 nm, which is in accordance with the literature [45]. The inset of Fig. 7a shows that the PL emission intensity of pure InVO₄ is higher than that of g-C₃N₄/InVO₄ composites. It indicates that heterojunction structure can enhance the separation efficiency of photo-generated charge carriers significantly. Moreover, the PL emission intensity of BCN/NI-50 is higher than that of RCN/SI-50 (Fig. 7b), suggesting that the recombination of photo-induced electron-hole pairs in the g-C₃N₄ nanorod/InVO₄ hollow sphere is inhibited more effectively. The special nanostructure and large contact area between g-C₃N₄ nanorod and InVO₄

hollow spheres made photo-generated charge carriers transfer easy. Time-resolved fluorescence decay spectra of CN, BCN/NI-50 and RCN/SI-50 were also recorded to understand the photophysical behaviors of photo-generated charge carriers, as shown in Fig. S3. The fluorescent intensities of both samples decay exponentially. Fitting the decay spectrum shows three radiative lifetimes with different percentages as given in Table S1. All of the three kinds of lifetime of charge carriers in RCN/SI-50 are the highest. Besides, RCN/SI-50 has a higher average charge carrier lifetime of 8.4 ns than that of 8.1 ns belonged to BCN/NI-50. The charge carriers with prolonged lifetime in RCN/SI-50 indicate a higher probability of their involvement in photocatalytic reactions before recombination.

3.4. Photocatalytic activities

Fig. 8a shows the photocatalytic degradation of methylene blue (MB) over various samples under visible light irradiation ($\lambda > 420$ nm), and the blank indicates that MB is stable under visible light irradiation if there is no photocatalyst present. CN and pure InVO₄ show weak photocatalytic activities owing to rapid recombination of photo-generated charge carriers and low charge transfer ability. While the sample of RCN/SI-50 with good nanorod/hollow sphere composite structure exhibits the highest photocatalytic activities. Compared with RCN/SI-50, a common g-C₃N₄/InVO₄ composite (BCN/NI-50) shows relatively lower photocatalytic activity. The photocatalytic decomposition kinetics of the as prepared sample is fitted by a pseudo-first-order model, which is depicted by the following equation:

$$\ln(C_0/C) = kt$$

where C₀ and C are the MB concentrations in solution at times 0 and t respectively, and k is the apparent first-order rate constant. As shown in Fig. 8b, RCN/SI-50 shows the highest photocatalytic decomposition rate of 0.400 h⁻¹ which is 25, 16.67 and 1.91 times higher than that of CN, pure InVO₄ and BCN/NI-50 respectively. Colorless antibiotic TC was also served as a target pollutant for photocatalytic degradation reaction. As displayed in Fig. 8c and d, the sample of RCN/SI-50 also shows the highest photocatalytic degradation with a rate of 0.226 h⁻¹ which is 2.5, 6.84 and 1.68 times higher than that of CN, pure InVO₄ and BCN/NI-50 respectively. The results indicate that such unique g-C₃N₄ nanorod/InVO₄ hollow sphere nanostructure can significantly enhance photocatalytic activity, owing to higher separation efficiency of photogenerated charge carriers and visible light harvesting ability, and the results are in accordance with DRS and PL analysis.

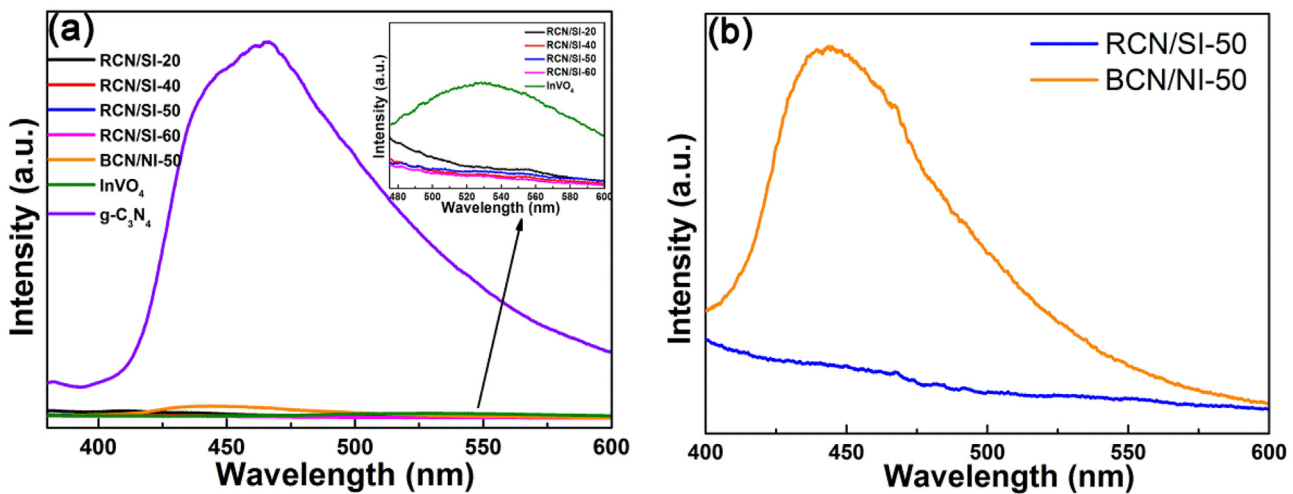


Fig. 7. PL spectra of (a) CN, pure InVO₄ and g-C₃N₄/InVO₄ composites, (b) RCN/SI-50 and BCN/NI-50.

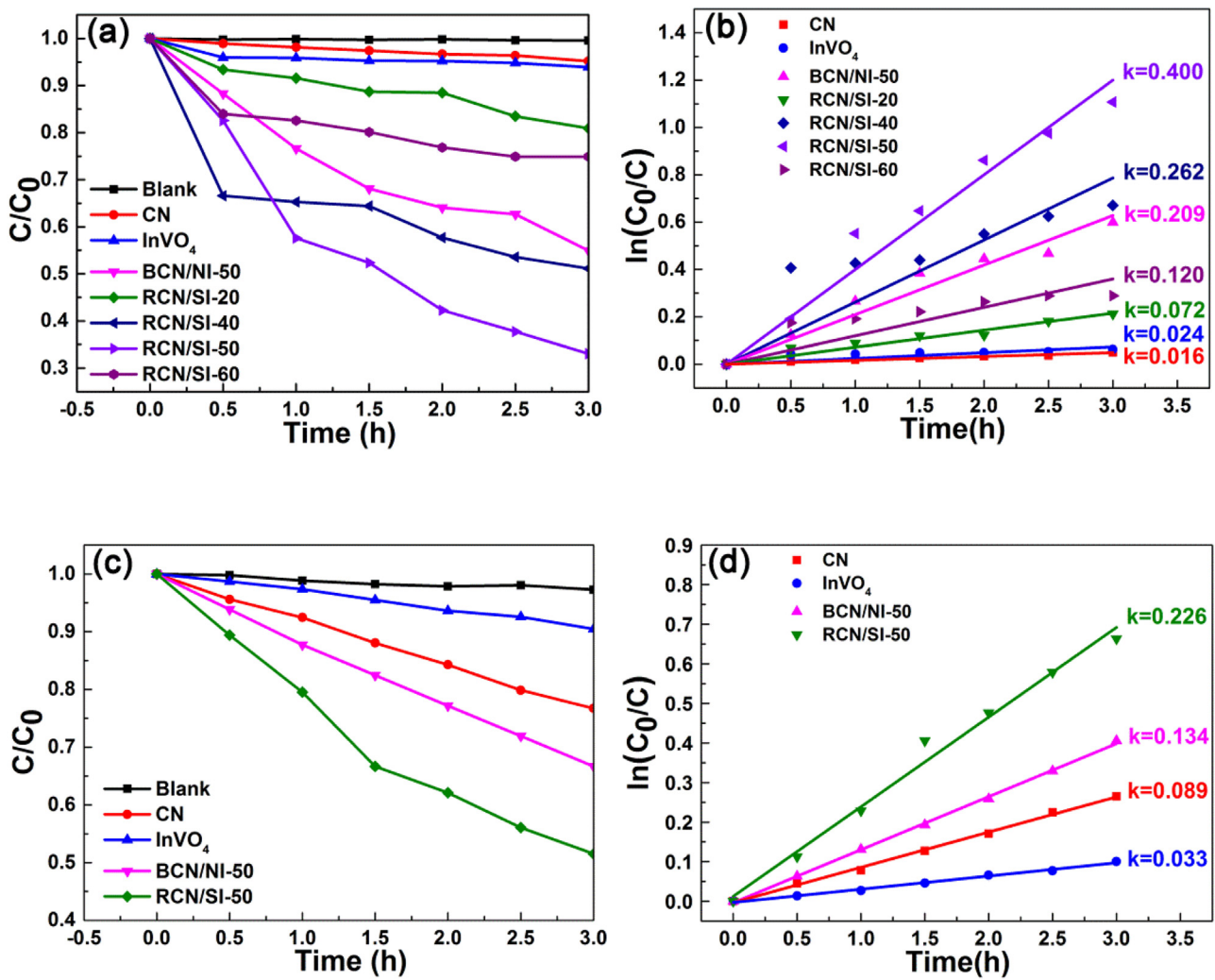


Fig. 8. Photocatalysis analysis of the as-prepared samples: (a) and (b) photocatalytic degradation of MB and the corresponding kinetics; (c) and (d) photocatalytic degradation of TC and the corresponding kinetics.

3.5. Photoelectrochemical properties

The electrochemical experiments have been conducted to further investigate the photogenerated charge transfer and separation

behaviors. EIS Nyquist plots of CN, BCN/NI-50 and RCN/SI-50 electrodes in a 0.5 M Na₂SO₄ aqueous solutions before and after visible-light irradiation are shown in Fig. 9a. A smaller arc radius of the EIS Nyquist plot suggests an effective separation of photo-

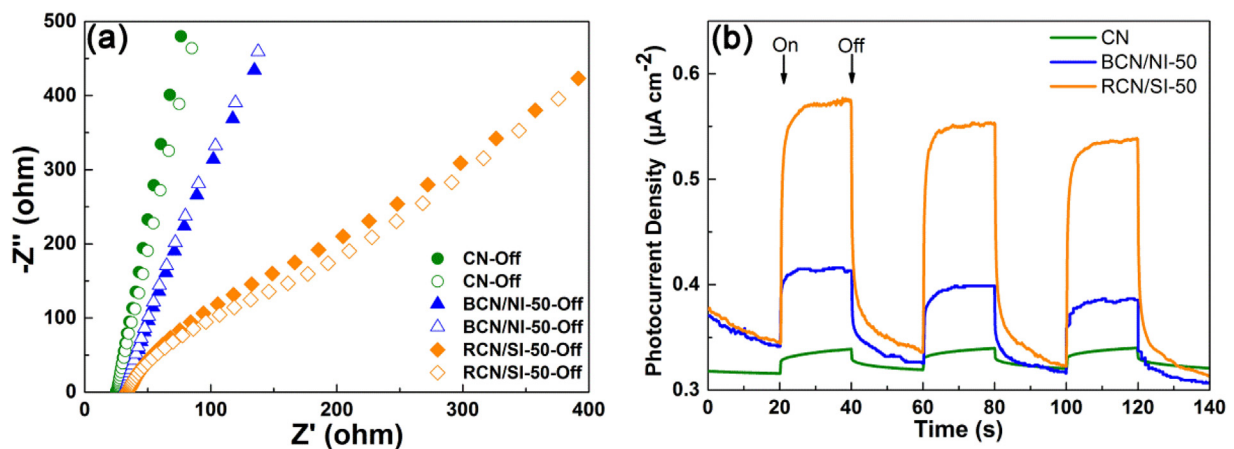


Fig. 9. Photoelectrochemical properties of CN, BCN/NI-50 and RCN/SI-50: (a) electrochemical impedance spectroscopy Nyquist plots with light on and off. (b) periodic ON/OFF photocurrent response in 0.5 M Na_2SO_4 electrolyte under visible-light irradiation ($\lambda > 420 \text{ nm}$, 300 W Xe lamp).

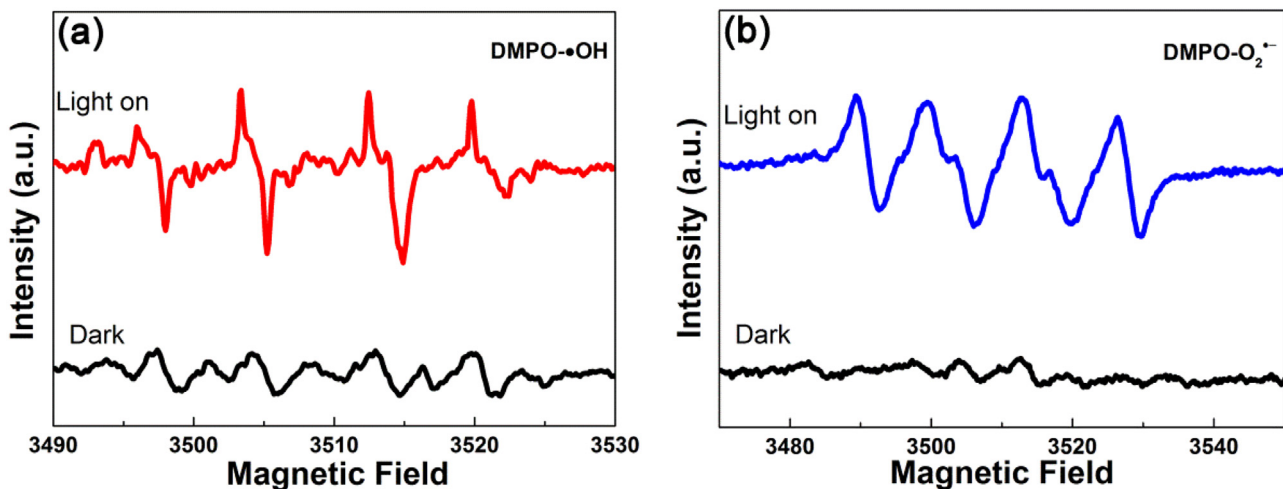


Fig. 10. DMPO spin-trapping ESR spectra under visible light irradiation ($\lambda > 420 \text{ nm}$) for 300 s in (a) aqueous solutions for $\cdot\text{OH}$ and (b) methanol solutions for $\text{O}_2^{\bullet-}$.

generated electron-hole pairs and fast interfacial charge transfer [46,47]. The arc radius on EIS Nyquist plot of BCN/NI-50 is smaller than that of CN. Meanwhile, the arc radius on EIS Nyquist plot of RCN/SI-50 with g-C₃N₄ nanorod/InVO₄ hollow sphere nanostructure is much smaller than that of common g-C₃N₄/InVO₄ composite (BCN/NI-50). Moreover, the RCN/SI-50 also exhibits the highest photocurrent density (Fig. 9b), indicating a strong ability of generation and transfer of photo-generated charge carriers [48,49]. Hence, it can be proved that the unique g-C₃N₄ nanorod/InVO₄ hollow sphere nanostructure can dramatically increase the separation and transfer efficiency of photo-generated carriers in the system, thereby achieving the obvious enhancement of photocatalytic activity.

3.6. Photocatalytic activity enhancement mechanism

DMPO spin-trapping ESR spectra were recorded to investigate the active radicals which were involved in the degradation reaction [50]. As displayed in Fig. 10, both of the characteristic signal of •OH radicals and $\text{O}_2^{\bullet-}$ radicals can be detected after visible-light irradiation, indicating the formation of •OH and $\text{O}_2^{\bullet-}$. Moreover, Isopropanol (IPA, •OH quencher), and benzoquinone (BQ, $\text{O}_2^{\bullet-}$ quencher) were introduced into MB photocatalytic degradation reaction system to further elucidate the photocatalytic mechanism. As shown in Fig. S4, different scavengers have different effects on

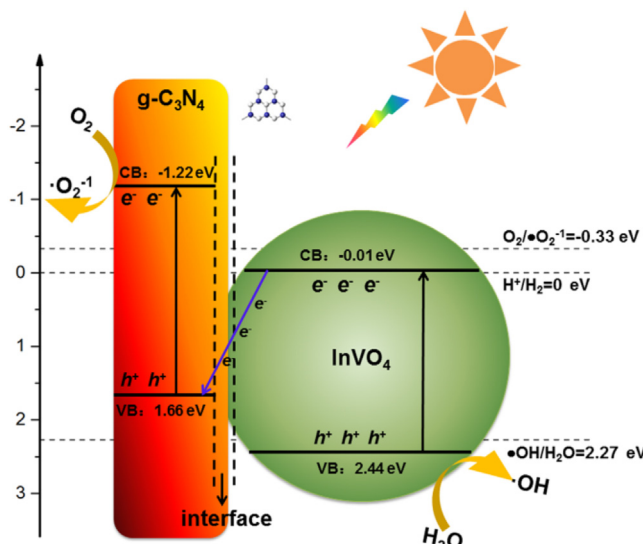
the degradation of MB over RCN/SI-50. The degradation of MB is inhibited significantly in the presence of BQ, but only little decline when IPA is added. These results suggest that the crucial reactive species is $\text{O}_2^{\bullet-}$ rather than •OH, although both of them are generated during the reaction.

The energy band positions of valence band (VB) and conduction band (CB) can be calculated by the following equations:

$$E_{CB} = X - E_e - \frac{1}{2}E_g$$

$$E_{VB} = E_{CB} + E_g$$

Where X is the absolute electronegativity of the semiconductor, E_e is the energy of free electrons on the hydrogen scale (4.5 eV) and E_g is the band gap of the semiconductor. According to the equation and DRS analysis, the CB and VB potentials of g-C₃N₄ can be calculated to be -1.22 eV and 1.66 eV. Similarly, the CB and VB potentials of InVO₄ can be determined as -0.01 eV and 2.44 eV respectively, which is nearly consistent with the literature [43]. According to the traditional charge carriers transfer mechanism, the photo-generated electrons prefer to migrate from the CB of g-C₃N₄ to the CB of InVO₄. Meanwhile, the holes in the VB of InVO₄ will transfer to the VB of g-C₃N₄. If so, electrons will accumulate in the CB of InVO₄ with potential of -0.01 eV, therefore losing the ability of reducing oxygen to form $\text{O}_2^{\bullet-}$ ($\text{O}_2/\text{O}_2^{\bullet-} = -0.33 \text{ eV}$ per



Scheme 2. Electron-hole pairs separation and transfer mechanism in $\text{g-C}_3\text{N}_4$ nanorod/InVO₄ hollow sphere photocatalyst under visible-light irradiation.

NHE) [51]. But this deduction is inconsistent with the results of ESR/DMPO probe test and trapping experiment.

Based on the results above, a Z-scheme transfer mechanism is proposed to elucidate the migration process of photo-generated charge carriers. As shown in **Scheme 2**, both $\text{g-C}_3\text{N}_4$ and InVO₄ can be excited by visible-light irradiation. Simultaneously, the photo-generated electrons in the CB of InVO₄ will migrate into the VB of $\text{g-C}_3\text{N}_4$. The photo-generated electrons of $\text{g-C}_3\text{N}_4$ will remain in the CB with more negative potentials to produce $\text{O}_2^{\bullet-}$, meanwhile, holes of InVO₄ will remain in the VB with more positive potentials to yield $\cdot\text{OH}$. Thus, high separation efficiency of electron-hole pairs is achieved due to this Z-scheme transfer mechanism. Moreover, nanorod structure of $\text{g-C}_3\text{N}_4$ can accelerate inhibiting the transfer of photo-generated carriers, and thus further facilitate separation efficiency of electron-hole pairs [52].

4. Conclusions

In summary, a facile and template-free method, which combines heterojunction constructing with morphology controlling of $\text{g-C}_3\text{N}_4$ in one step, was successfully developed to synthesize $\text{g-C}_3\text{N}_4$ nanorod/InVO₄ hollow sphere composites. This unique nanorod/hollow sphere nanostructure can promote the absorption for visible-light and result in low recombination efficiency of photo-generated electron-hole pairs through Z-scheme transfer mechanism, thereby achieving enhanced photocatalytic activity compared with $\text{g-C}_3\text{N}_4$, InVO₄ and common $\text{g-C}_3\text{N}_4/\text{InVO}_4$ composites, respectively. Moreover, this fabrication method may open up new opportunities for further studies of other $\text{g-C}_3\text{N}_4$ based composites with controllable morphologies and high photocatalytic activity.

Acknowledgements

This work is supported by The National Key Research and Development Program of China (No. 2016YFB0701100).

Appendix A. Supplementary data

Supplementary data associated with this article can be found, in the online version, at <http://dx.doi.org/10.1016/j.apcatb.2017.05.015>.

References

- [1] A.J. Bard, *Science* 207 (1980) 139–144.
- [2] M.R. Hoffmann, S.T. Martin, W. Choi, D.W. Bahnemann, *Chem. Rev.* 95 (1995) 69–96.
- [3] J. Liu, Y. Liu, N. Liu, Y. Han, X. Zhang, H. Huang, Y. Lifshitz, S.T. Lee, J. Zhong, Z. Kang, *Science* 347 (2015) 970–974.
- [4] Y. Zheng, J. Liu, J. Liang, M. Jaroniec, S.Z. Qiao, *Energy Environ. Sci.* 5 (2012) 6717–6731.
- [5] Y. Wang, X. Wang, M. Antonietti, *Angew. Chem. Int. Ed.* 51 (2012) 68–89.
- [6] Q. Liang, Z. Li, X. Yu, Z.H. Huang, F. Kang, Q.H. Yang, *Adv. Mater.* 27 (2015) 4634–4639.
- [7] X. Wang, K. Maeda, A. Thomas, K. Takanabe, G. Xin, J.M. Carlsson, K. Domen, M. Antonietti, *Nat. Mater.* 8 (2009) 76–80.
- [8] G. Zhang, M. Zhang, X. Ye, X. Qiu, S. Lin, X. Wang, *Adv. Mater.* 26 (2014) 805–809.
- [9] G. Liu, T. Wang, H. Zhang, X. Meng, D. Hao, K. Chang, P. Li, T. Kako, J. Ye, *Angew. Chem.* 127 (2015) 13765–13769.
- [10] Y. Guo, J. Li, Z. Gao, X. Zhu, Y. Liu, Z. Wei, W. Zhao, C. Sun, *Appl. Catal. B* 192 (2016) 57–71.
- [11] H. Zhao, S. Chen, X. Quan, H. Yu, H. Zhao, *Appl. Catal. B* 194 (2016) 134–140.
- [12] F. Dong, Z. Wang, Y. Sun, W.K. Ho, H. Zhang, *J. Colloid Interface Sci.* 401 (2013) 70–79.
- [13] A.B. Jorge, D.J. Martin, M.T. Dhanoa, A.S. Rahman, N. Makwana, J. Tang, A. Sella, F. Cora, S. Firth, J.A. Darr, P.F. McMillan, *J. Phys. Chem. C* 117 (2013) 7178–7185.
- [14] P. Niu, L. Zhang, G. Liu, H.M. Cheng, *Adv. Funct. Mater.* 22 (2012) 4763–4770.
- [15] L. Chen, D. Huang, S. Ren, T. Dong, Y. Chi, G. Chen, *Nanoscale* 5 (2013) 225–230.
- [16] H. Wang, X. Yuan, H. Wang, X. Chen, Z. Wu, L. Jiang, W. Xiong, G. Zeng, *Appl. Catal. B* 193 (2016) 36–46.
- [17] Y. Zhang, T. Mori, J. Ye, M. Antonietti, *J. Am. Chem. Soc.* 132 (2010) 6294–6295.
- [18] J. Li, B. Shen, Z. Hong, B. Lin, B. Gao, Y. Chen, *Chem. Commun.* 48 (2012) 12017–12019.
- [19] Q. Kang, J. Cao, Y. Zhang, L. Liu, H. Xu, J. Ye, *J. Mater. Chem. A* 1 (2013) 5766–5774.
- [20] M. Zhang, W. Luo, Z. Wei, W. Jiang, D. Liu, Y. Zhu, *Appl. Catal. B* 194 (2016) 105–110.
- [21] Q. Liu, T. Chen, Y. Guo, Z. Zhang, X. Fang, *Appl. Catal. B* 193 (2016) 248–258.
- [22] N. Cheng, J. Tian, Q. Liu, C. Ge, A.H. Qusti, A.M. Asiri, A.O. Al-Youbi, X. Sun, *ACS Appl. Mater. Interfaces* 5 (2013) 6815–6819.
- [23] J. Fu, B. Chang, Y. Tian, F. Xi, X. Dong, *J. Mater. Chem. A* 1 (2013) 3083–3090.
- [24] S. Kumar, T. Surendar, A. Baruah, V. Shanker, *J. Mater. Chem. A* 1 (2013) 5333–5340.
- [25] T. Li, L. Zhao, Y. He, J. Cai, M. Luo, J. Lin, *Appl. Catal. B* 129 (2013) 255–263.
- [26] X. Zhang, H. Wang, H. Wang, Q. Zhang, J. Xie, Y. Tian, J. Wang, Y. Xie, *Adv. Mater.* 26 (2014) 4438–4443.
- [27] X.H. Li, X. Wang, M. Antonietti, *Chem. Sci.* 3 (2012) 2170–2174.
- [28] Y. Cui, Z. Ding, X. Fu, X. Wang, *Angew. Chem. Int. Ed.* 51 (2012) 11814–11818.
- [29] S. Yang, Y. Gong, J. Zhang, L. Zhan, L. Ma, Z. Fang, R. Vajtai, X. Wang, P.M. Ajayan, *Adv. Mater.* 25 (2013) 2452–2456.
- [30] J. Sun, J. Zhang, M. Zhang, M. Antonietti, X. Fu, X. Wang, *Nat. Commun.* (2012) 1139.
- [31] X.H. Li, J. Zhang, X. Chen, A. Fischer, A. Thomas, M. Antonietti, X. Wang, *Chem. Mater.* 23 (2011) 4344–4348.
- [32] J. Ye, Z. Zou, M. Oshikiri, A. Matsushita, M. Shimoda, M. Imai, T. Shishido, *Chem. Phys. Lett.* 356 (2002) 221–226.
- [33] K. Rakesh, S. Khaire, D. Bhange, P. Dhanasekaran, S.S. Deshpande, S.V. Awate, N.M. Gupta, *J. Mater. Sci.* 46 (2011) 5466.
- [34] L. Chen, Y. Liu, Z. Lu, D. Zeng, J. *Colloid Interface Sci.* 295 (2006) 440–444.
- [35] L. Zhang, H. Fu, C. Zhang, Y. Zhu, *J. Solid State Chem.* 179 (2006) 804–811.
- [36] L. Liao, Q. Zhang, Z. Su, Z. Zhao, Y. Wang, Y. Li, X. Lu, D. Wei, G. Feng, Q. Yu, X. Cai, J. Zhao, Z. Ren, H. Fang, F.R. Hernandez, S. Baldelli, J. Bao, *Nat. Nanotechnol.* 9 (2014) 69–73.
- [37] S. Sun, W. Wang, D. Li, L. Zhang, D. Jiang, *ACS Catal.* 4 (2014) 3498–3503.
- [38] B. Hu, F. Cai, T. Chen, M. Fan, C. Song, X. Yan, W. Shi, *ACS Appl. Mater. Interfaces* 7 (2015) 18247–18256.
- [39] Y. Shang, X. Chen, W. Liu, P. Tan, H. Chen, L. Wu, C. Ma, X. Xiong, J. Pan, *Appl. Catal. B* 204 (2017) 78–88.
- [40] J. Liu, H. Xu, Y. Xu, Y. Song, J. Lian, Y. Zhao, L. Wang, L. Huang, H. Ji, H. Li, *Appl. Catal. B* 207 (2017) 429–437.
- [41] Z. Yan, Z. Sun, X. Liu, H. Jia, P. Du, *Nanoscale* 8 (2016) 4748–4756.
- [42] J. Yan, H. Wu, H. Chen, L. Pang, Y. Zhang, R. Jiang, L. Li, S.F. Liu, *Appl. Catal. B* 194 (2016) 74–83.
- [43] Y. Yan, F. Cai, Y. Song, W. Shi, *Chem. Eng. J.* 233 (2013) 1–7.
- [44] X. Yang, F. Qian, G. Zou, M. Li, J. Lu, Y. Li, M. Bao, *Appl. Catal. B* 193 (2016) 22–35.
- [45] J. Shen, H. Yang, Q. Shen, Y. Feng, *J. Mater. Sci.* 48 (2013) 7574–7580.
- [46] X. Bai, L. Wang, Y. Wang, W. Yao, Y. Zhu, *Appl. Catal. B* 152 (2014) 262–270.
- [47] X. Du, G. Zou, Z. Wang, X. Wang, *Nanoscale* 7 (2015) 8701–8706.
- [48] K. Lv, X. Li, K. Deng, J. Sun, X. Li, M. Li, *Appl. Catal. B* 95 (2010) 383–392.
- [49] Z. Huang, Q. Sun, K. Lv, Z. Zhang, M. Li, B. Li, *Appl. Catal. B* 164 (2015) 420–427.
- [50] Y. Li, K. Lv, W. Ho, F. Dong, X. Wu, Y. Xia, *Appl. Catal. B* 202 (2017) 611–619.
- [51] S. Wang, D. Li, C. Sun, S. Yang, Y. Guan, H. He, *Appl. Catal. B* 144 (2014) 885–892.
- [52] X. Bai, L. Wang, R. Zong, Y. Zhu, *J. Phys. Chem. C* 117 (2013) 9952–9961.